Refining Energy Levels in ReS₂ Nanosheets by Low-Valent Transition-Metal Doping for Dual-Boosted Electrochemical Ammonia/Hydrogen Production

Feili Lai, Nan Chen, Xiaobin Ye, Guanjie He, Wei Zong, Katherine B. Holt, Bicai Pan, Ivan P. Parkin, Tianxi Liu,* Renjie Chen*

Dr. F. Lai, W. Zong, Prof. T. Liu

Key Laboratory of Synthetic and Biological Colloids, Ministry of Education, School of Chemical and Material Engineering, Jiangnan University, Wuxi 214122, P. R. China

Email: txliu@dhu.edu.cn

Dr. N. Chen, Prof. R. Chen

School of Materials Science & Engineering, Beijing Institute of Technology, Beijing, 100081, China

Email: chenrj@bit.edu.cn

Dr. G. He, Prof. K. Holt, Prof. I. Parkin,

Christopher Ingold Laboratory, Department of Chemistry, University College London, 20 Gorden Street, London WC1H 0AJ, UK

X. Ye, Prof. B. Pan

Hefei National Laboratory for Physical Science at the Microscale, University of Science and Technology of China, Anhui 230026, China

Abstract:

Electrocatalytic nitrogen reduction reaction (NRR) and hydrogen evolution reaction (HER) may provide intriguing approaches to nitrogen fixation and hydrogen production under ambient conditions, which need discover efficient and stable catalysts to light up the "green chemistry" future. However, it often forms bottlenecks on N_2/H_2O activation, the very first step of NRR/HER, by energetic electron injection from the surface of electrocatalysts. Herein, we report that the bottlenecks for both NRR and HER can be well tackled by engineering the energy level *via* low-valent transition-metal doping,

simultaneously, where ReS_2 is employed as a model platform to prove the concept. The doped low-valent transition-metal domains (e.g. Fe, Co, Ni, Cu, Zn) in ReS_2 provide more active sites for N_2/H_2O chemisorption and electron transfer, not only weakening the $N\equiv N$/O-H bonds for easier dissociation through proton coupling, but also elevating d-band center toward the Fermi level with more electron energy for N_2/H_2O reduction. As a result, we found that iron-doped ReS_2 nanosheets wrapped nitrogen-doped carbon nanofiber (Fe-ReS_2@N-CNF) catalyst exhibits superior electrochemical activity with 8-fold higher ammonia production yield of 80.4 μg h^{-1} mg$^{-1}_{cat.}$, and lower onset overpotential of 146 mV and Tafel slope of 63 mV dec^{-1}, when comparing with the pristine ReS_2.

Ammonia (NH_3) is an indispensable carbon-free chemical to agriculture and other products,[1-3] as well as potential carrier for hydrogen storage due to its high hydrogen density and liquefiable feature.[4,5] However, the chemical inertness of dinitrogen (large bond energy of 940.95 kJ mol^{-1}),[6,7] makes it a "Cadmean victory" to convert N_2 into NH_3. For instance, the famous reaction for industrial ammonia production is known as Haber-Bosch process, relying on iron-based catalysts and rigorous operating conditions (673-873 K, 20-40 MPa),[8,9] which almost accounts for 1% of the worldwide energy consumption and 1.6% of the total global CO_2 emission.[10]

In order to promote the progress of "green chemistry", a clean, safe, and sustainable NH_3 synthesis route is in an urgent need. Electrochemical nitrogen reduction reaction (NRR) has gradually attracted much attention, and been regarded as an alternative approach.[11-14] As an inevitably overwhelming rival, hydrogen evolution reaction (HER) is always wanted to be impeded, making it a key issue to find a reasonable way to enhance N species adsorption on the surface of catalyst instead of H species. For instance, Ling et al. put forward a reticular chemistry approach by exploiting MOF's water-repelling and molecular-concentrated effects to overcome HER-imposed bottlenecks, achieving both excellent NRR selectivity (~90%) and boosted Faradaic efficiency by 10 percentage points.[15] Recently, Yan et al. reported a strategy to simultaneously promote NRR selectivity and activity by

using bismuth nanocrystals and potassium cations, the Faradaic efficiency of which was achieved as 66%.[16] Yan et al. also proposed it can suppress the HER process and improve the Faradaic efficiency of NRR to 56.55% by positively shifting the reaction potential and using single-atom iron as electrocatalyst.[17] To our knowledge, however, traditional Haber-Bosch process will still be the main route for NH_3 production in the foreseeable future with a large amount usage of H_2 by steam reforming of fossil fuels, where HER would be a more attractive choice for renewable H_2 resource. In fact, the majority used hydrogen gas for Haber-Bosch process would go through a series of chemical treatment processes under high temperature, while less than 4% of the total H_2 gas comes from sustainable and mild electrocatalysis of water. Therefore, it would be also another possible perspective to explore dual-enhanced electrocatalysts for both ammonia and hydrogen production, as it is still difficult to suppress the HER process well for the majority electrocatalysts.

Bearing this in mind, rhenium disulfide (ReS_2) is recently discovered as next-generation transition metal dichalcogenide (TMD) materials for high-efficient electrocatalysis.[18,19] It is mainly attributed to their layered structure with weak van der Waals interactions between individual sandwiched layers,[20,21] and anisotropic structure with two-dimensional morphology to provide not only large specific surface area but also two-dimensional permeable channels for reactant adsorption/transport.[22] In the past few years, abundant effort has been made to promote the development of TMD-based electrocatalysts for both nitrogen reduction reaction and hydrogen evolution reaction.[23-25] In contrast with other TMD materials (such as MoS_2, $MoSe_2$, WS_2, and WSe_2), ReS_2 possesses a very weak interlayer coupling,[25-27] thus leading to an enhanced reactant diffusion into its deep interlayer space for better NRR/HER processes. Besides that, traces of transition-metal doping, particularly for low-valent domains (such as Fe^{3+}, Co^{2+}, Ni^{2+}, Cu^{2+}, Zn^{2+}),[28-30] in atomically ordered ReS_2 nanosheets can disturb its crystalline lattice to expose more active sites for electrocatalysis. However, several significant issues in low-valent transition-metal doped ReS_2 nanosheets are still rarely reported and

urgently needed to be addressed and solved, namely, how does transition-metal incorporate into ReS_2, and where are the real electrocatalytic sites for NRR/HER?

Therefore, here we employ low-valent $Fe^{3+}/Co^{2+}/Ni^{2+}/Cu^{2+}/Zn^{2+}$ salts deliberately for coprecipitation with ReO_4^- salt. By this, M^{4+}-positioned Re could be replaced by low-valent transition-metal species (e.g. Fe, Co, Ni, Cu, Zn). The density functional theory (DFT) calculation firstly reveals that the energy level of ReS_2 can be well tuned by doping engineering with enhanced charge density around the low-valent cations. Taking iron-doped ReS_2 nanosheets wrapped nitrogen-doped carbon nanofiber (Fe-ReS_2@N-CNF) catalyst as an example, it exhibits superior electrochemical activity with an 8-fold higher ammonia production yield rate of 80.4 µg h^{-1} mg$^{-1}_{cat.}$ for NRR, and lower onset overpotential of 146 mV and Tafel slope of 63 mV dec^{-1} for HER, when comparing with the pristine ReS_2. The deep mechanisms for NRR/HER processes are further discovered by in-situ spectroscopic characterization together with DFT studies that low-valent Fe domain is beneficial to providing more active sites for N_2/H_2O chemisorption and weakening the N≡N/O-H bonds for easier dissociation through proton coupling. These results clearly demonstrate the important role of low-valent transition-metal doping engineering on optimizing ReS_2-based NRR/HER electrocatalyst, which provides a novel but general route for green synthesis of NH_3 production.

Foreseen by computational study firstly, the pristine ReS_2 semiconductor shows a wide energy gap (E_g) of 1.31 eV (**Figure 1a**) as direct-band gap. This high E_g will certainly hinder the catalyst activation with inefficient electron transition. Interestingly, the other five kinds of optimized ReS_2 models were constructed by doping 5% low-valent transition-metals (e.g. Fe, Co, Ni, Co and Zn), denoted as Fe-ReS_2 (**Figure 1b**), Co-ReS_2 (**Figure 1c**), Ni-ReS_2 (**Figure 1d**), Cu-ReS_2 (**Figure 1e**), and Zn-ReS_2 (**Figure 1f**), respectively. As a result, we found the E_g values of these doped ReS_2 samples significantly decreased to around 1.03 eV as indirect-band gaps, demonstrating it a feasible strategy for superior electron excitation of transition-metal doped ReS_2. The well reduced energy gap is attributed to the impurity band after doping of transition-metals, which can be either in the gap or in the

valence/conduction band. Here, the first-principle calculations show that impurity band will live in the gap of transition-metal doped ReS_2, therefore the gap is decreased. Meanwhile, this may also be originated from the activate ReS_2 atomic surface with charge redistribution, especially centered around low-valance transition-metal doped domains (**Figure 1&S1**),[31] which can be regarded as highly active electrocatalysts.

Inspired by the above theoretical results, iron-doped ReS_2 nanosheets wrapped nitrogen-doped carbon nanofiber (Fe-ReS_2@N-CNF) is firstly chosen as the key model system to investigate the benefits of low-valent transition-metal doping engineering. The samples are synthesized *via* a N-CNF templated hydrothermal method,[32] in which Fe atoms are doped into ReS_2 lattice using $FeCl_3 \cdot 6H_2O$ as a precursor as schematically illustrated in **Figure 2a**. Firstly, the typical scanning electron microscopy (SEM) image of N-CNF is displayed in **Figure 2b** with average diameter of 30-60 nm, proving that the heteroatom doping process for nitrogen atoms would not affect its morphology (**Figure S5**) and non-crystalline property (**Figure S6**). The nitrogen-rich carbon surface is also beneficial to the adsorption of ReO_4^-/Fe^{3+} precursors for epitaxial growth of Fe-ReS_2 nanosheets. **Figure 2c-e** reveal the morphology of Fe-ReS_2@N-CNF by SEM and transmission electron microscopy (TEM), highlighting a feature of uniform Fe-ReS_2 nanosheets covered hybrid carbon nanofiber with ultrafine diameter of ~85 nm and length extending to several micrometers. This hybrid strategy is beneficial to solving the difficult problem of Fe-ReS_2 aggregations (**Figure S7**), leading to significantly increased specific surface area from 12.1 to 24.6 cm^2 g^{-1} (**Figure S8**). As displayed in high-resolution TEM (HRTEM) image (**Figure 2f**), the iron-doped ReS_2 nanosheets with a spacing of 0.62 nm can be assigned to (001) planes, indicating that the Fe-ReS_2 mainly grow along [001] direction. Energy-dispersive X-ray spectroscopy (EDS) mapping is further employed to ascertain the doping of Fe and N elements on Fe-ReS_2@N-CNF-5, revealing the uniform Fe and N doping (**Figure 2g**). X-ray diffraction (XRD) exhibits the same Bragg reflections of Fe-ReS_2@N-CNF-5 and non-doped

ReS$_2$@N-CNF (**Figure 2h**), implying no structural deformation caused by low-valent Fe substitution of Re^{4+}.

X-ray photoelectron spectroscopy (XPS) is further applied to understand the chemical states and elemental compositions in the Fe-ReS$_2$@N-CNF-5. The binding energies of the Re^{4+} 4$f_{7/2}$ and 4$f_{5/2}$ electron peaks in Fe-ReS$_2$@N-CNF-5 are 41.0 eV and 44.4 eV, respectively (**Figure 3a**).[33] As shown in **Figure 3b**, two characteristic peaks being located at 162.4 eV and 163.4 eV in Fe-ReS$_2$@N-CNF-5 are detected for the bonding configurations of S, corresponding to the core 2$p_{3/2}$ and 2$p_{1/2}$ level peaks of S^{2-}, respectively.[34] All these above results are consistent with values for ReS$_2$@N-CNF, indicating the immeasurable changes for chemical states of Re and S elements after doping iron atoms in Fe-ReS$_2$@N-CNF-5. Three types of pyridinic N (398.4 eV), pyrrolic N (400.3 eV), and graphitic N (401.1 eV) are identified from Fe-ReS$_2$@N-CNF-5 (**Figure 3c**), manifesting the successful incorporation of N atoms in the carbon nanofiber template. Meanwhile, the high pyridinic N content in Fe-ReS$_2$@N-CNF-5 can also promote the following ammonia production.[35] The binding energies of the Fe 2$p_{3/2}$ and Fe 2$p_{1/2}$ electron peaks in Fe-ReS$_2$@N-CNF-5 are 708.1 eV and 721.2 eV (**Figure 3d**), respectively, confirming the successful incorporation of Fe atoms in ReS$_2$ structure. In this instance, an obviously negative shift of binding energy for the Fe 2$p_{3/2}$ electron is observed when compared with other iron compounds, such as binding energies of Fe 2$p_{3/2}$ in Fe$_2$O$_3$ (710.1 eV), FeCl$_2$ (710.7 eV), and FeCl$_3$ (711.6 eV).[36] It can be ascribed to the bonding hybridization of Fe atom with its neighbor atoms, leading to the decreased oxidation state of Fe. After incorporating low-valent Fe element in ReS$_2$ nanosheets, the density distribution in Fe-ReS$_2$ is significantly destabilized to Fe-doped domains (*inset* in **Figure 3d**), due to the structural heterogeneity-leaded charge rearrangement. Furthermore, the quantitative analysis of XPS spectra (**Figure S9**) demonstrates the chemical formula of 5 mol % Fe-doped ReS$_2$ nanosheets can be fixed to Fe$_{0.073}$Re$_{0.991}$S$_2$ (**Table S1**).

Upon confirming the electronic structure of low-valent Fe doped ReS$_2$ compound, we are now in a position to evaluate the efficacy of as-obtained 5 mol % transition-metal doped ReS$_2$ nanosheets

wrapped nitrogen-doped carbon nanofiber (Fe/Co/Ni/Cu/Zn-ReS$_2$@N-CNF-5) for electrochemical HER/NRR performance, which were tested under 0.1 M Na$_2$SO$_4$ solution with continuous N$_2$ bubbling. As shown in the polarization curves (**Figure 4a**) and Tafel plots (**Figure 4b**), the low-valent transition-metal doping could moderately improve the HER activity of non-doped ReS$_2$@N-CNF (**Table S2**). Taking Fe-ReS$_2$@N-CNF as an example, it shows lower onset overpotential (η = 146 mV, the onset overpotential is defined as the difference between the reversible potential of the couple H$_2$/H$^+$ and the potential where electrocatalysis occurs) and Tafel slope (63 mV dec^{-1}) than those in ReS$_2$@N-CNF (η = 200 mV; 87 mV dec^{-1}), implying its superiority to accelerate the hydrogen evolution reaction by low-valent transition-metal doping engineering. As an efficient conductive-frame, nitrogen-doped carbon nanofiber is also beneficial for the electron transfer along the interface of N-CNF and ReS$_2$ outer layer, leading to the enhanced HER performance (**Figure S12**). Fe-ReS$_2$@N-CNF-5 also shows remarkable durability (**Figure S13**), without dramatic change of the LSV curve after 5000 cycles. Apart from positive effect of low-valent transition-metal doping engineering in HER activity, we also found it is useful in the improvement of nitrogen reduction reaction (NRR). As shown in **Figure 4c**, the maximum NH$_3$ yield rate (80.4 μg h^{-1} mg$^{-1}_{cat.}$) and Faradaic efficiency (FE = 12.3 %) of Fe-ReS$_2$@N-CNF-5 are much higher than those of non-doped ReS$_2$@N-CNF (10.3 μg h^{-1} mg$^{-1}_{cat.}$, FE = 9.9%) at -0.2 V versus reversible hydrogen electrode (RHE). In order to make the quantitative method for NH$_3$ yield rate more convincing, nuclear magnetic resonance (NMR) method was further applied (**Figure S20a**). Based on the corresponding fitted curve (**Figure S20b**), the NH$_3$ yield rate can be calculated to be 79.8 μg h^{-1} mg$^{-1}_{cat.}$, which approached to the NH$_3$ yield rate from indophenol blue method within the allowed error range, demonstrating the reliability of detection methods (NMR and indophenol blue methods). This enhanced NRR performance can also be observed in other low-valent transition-metal doped electrodes of Co/Ni/Cu/Zn-ReS$_2$@N-CNF-5 (**Figure S21 &Table S3**). To verify the source of ammonia production, NMR method was conducted as ^{15}N isotopic labeling experiments. As displayed in **Figure S22**, only ^{14}N triplets and ^{15}N doublets were observed in the

$^{14}NH_4^+$ and $^{15}NH_4^+$ productions, respectively, by using $^{14}N_2$ and $^{15}N_2$ as feeding gases, which demonstrate not only the purity of as-used $^{14}N_2$ gas but also the stable structure of Fe-ReS$_2$@N-CNF-5 electrocatalyst without escaped N atoms during NRR process. Meanwhile, it was revealed that the Fe-doping concentrations would be closely related with the corresponding NRR performance (especially for NH$_3$ yield), 5% Fe-doping amount would be a more proper concentration to release the best electrocatalytic activity for Fe-ReS$_2$ samples (**Figure S24**). Both the NH$_3$ yield rates and FE$_{NH3}$ values for Fe-ReS$_2$@N-CNF-5 are also well maintained with a stability retaining of ~99% after 10 continuous electrochemical NRR tests (**Figure 4d**). From the corresponding XPS spectra (**Figure S25**), the Fe-ReS$_2$@N-CNF-5 still maintains the same chemical states and elemental compositions after NRR stability test as the ones before electrocatalysis (**Figure 3**), demonstrating its excellent electrocatalytic stability for long-term usage. As shown in **Figure S26**, the sum of the amounts for generated NH$_3$ production (S2) and H$_2$ production (S1) equals the total supplied charge amount (S1 + S3), which indicates all the supplied charge was used to reduce neither N$_2$ gas nor H$_2$O molecules with a Faradaic efficiency of 87.7% for HER process. The rough agreement of the charge amount (S2 ≈ S3) between experimentally quantified gases (NH$_3$ and H$_2$) and calculated one suggests the total FE is 100% for the sum of NRR and HER without hydrazine generation (**Figure S28**).

These enhanced NRR and HER performances in Fe-ReS$_2$@N-CNF-5 can be attributed to the refined energy levels of ReS$_2$ nanosheets after low-valent transition-metal doping, as predicted by DFT calculations in **Figure 1**. Experimentally, ultraviolet photoelectron spectroscopy (UPS) was used to determine the values of energy level (difference between the vacuum and Fermi level) of Fe-ReS$_2$ and pure ReS$_2$ as 6.11 and 7.27 eV (**Figure 4e&Figure S29**), respectively, by subtracting the width of the He I UPS spectra at excitation energy of 21.22 eV. Compared with the energy level of non-doped ReS$_2$ nanosheets, the one of Fe-ReS$_2$ is properly shifted to approach the reduction potentials of H$_2$O and N$_2$ (**Figure 4f**), making the electron exchange process (**Figure S30**) easier between electrocatalyst and the reacting species.[30] Due to the increased energy levels of Fe-ReS$_2$ nanosheets, the energy required

for electron remove from the catalyst surface decreases, leading to the thermodynamically activated NRR and HER. In another perspective, the feasibility of electron transfer in low-valent transition-metal doped ReS_2 electrocatalysts would deliver lower onset overpotentials, demonstrating the Fe-ReS_2@N-CNF-5 a promised electrocatalyst for NRR and HER processes. Additionally, the incorporation of highly conductive N-CNF template is beneficial to increasing the electron transfer between two components in the Fe-ReS_2@N-CNF-5 for efficient reduction reaction as compared with that in Fe-ReS_2 bulk (**Figure S31**).

Apart from the perspective of thermodynamics, kinetics also plays a key role in these reactions. Attributing to N-CNF template and low-valance Fe doping, Fe-ReS_2@N-CNF-5 displays an increased number of electroactive sites (evidenced by the N_2 adsorption-desorption isotherms in **Figure S8** and optimized electronic structure in **Figure 3d**), leading to the optimal activation effect of H_3O^+ and N_2 reagents on catalyst surface. For the HER process (**Figure 5a**), the H_3O^+ molecule interacts between $Re^{\delta+}/Fe^{\delta+}\cdots O$ and $S^{\delta-}\cdots H$ synergistically, as the first volmer step ($H_2O + e^- \rightarrow H_{ads} + OH^-$). After the adsorption of another H_2O molecule, the H_2 gas generates by following one kind of desorption steps ($H_{ads} + H_2O + e^- \rightarrow H_2 + OH^-$ or $H_{ads} + H_{ads} \rightarrow H_2$). Revealed by DFT calculation further (**Figure S32**), the free energy value for H* (where * denotes as an adsorption site) is -0.36 eV for the pure ReS_2, but the water adsorption energy is up to 0.81 eV, which lead to the sluggish HER kinetics. Although the free energy value for H* in Fe-ReS_2 is relatively higher to be -0.49 eV, its water adsorption energy can be drastically reduced to 0.29 eV, indicating it thermodynamically favorable for water reduction on Fe-ReS_2 in neutral solution. To further investigate the nitrogen reduction reaction process (**Figure 5a**), in-situ surface-enhanced infrared absorption spectroscopy (SEIRAS) measurements were carried out for Fe-ReS_2@N-CNF-5 sample (**Figure 5b-d**). The IR bands at about 3420 and 1646 cm^{-1} (**Figure 5b**) match well with the O-H stretching and H-O-H bending of water molecules, respectively. Their positive shift with the decrease of applied potential from 0 to -0.3 V is attributed to the change of the adsorption configuration of water.[37] The peaks at 1554/1519, 1330 and 1102 cm^{-2} are attributed to

the H-N-H bending,[38,39] -NH$_2$ wagging,[13,40] and N-N stretching[41,42] of adsorbed N$_2$H$_y$ species, respectively. These results demonstrate that the nitrogen reduction reaction on Fe-ReS$_2$ follows an associative mechanism, instead of dissociative mechanism in the Haber-Bosch process,[43] with the simultaneous addition of hydrogen on N$_2$ to break the N≡N bond. The time-dependent SEIRAS spectra (**Figure 5d**) of Fe-ReS$_2$@N-CNF-5 catalyst at -0.2 V show similar absorption results with time goes, demonstrating its ultra-stable electrocatalysis. As reported in previous literature, enzymatic mechanism of N$_2$ fixation is more suitable for single-atom-embedded systems with lower energy barrier.[44,45] Therefore, the possible NRR mechanism is depicted in **Figure S33** with DFT calculation results in **Figure 5e-g**. All the reaction intermediates were bounded simultaneously to the surface Re atoms of both Fe-ReS$_2$ and ReS$_2$, while the Re atoms neighboring Fe atom showed higher activity for the reactions of N-related species (**Figure 5e&4f**). The calculation results further indicate the active sites in Fe-ReS$_2$ are located in the region near doped Fe atoms (especially for the Re atoms), which is corresponded with the ELF mappings (**Figure 1**) and destabilized density distribution (*inset* in **Figure 3d**). Furtherly revealed by the free energy diagram (**Figure 4g**), the adsorption energy of nitrogen on Fe-ReS$_2$ (-0.28 eV) is much smaller than that on ReS$_2$ (-0.04 eV), which demonstrates that nitrogen is prefer to be adsorbed and activated on the Fe-doped surface of Fe-ReS$_2$. Subsequently, six consecutive protonation and reduction processes were canvassed as N$_2$ (g)* → NNH* → HNNH* → HNNH$_2$* → H$_2$NNH$_2$* → NH$_2$* + NH$_3$ → NH$_3$ (**Table S4**). For the reaction pathway on ReS$_2$, the NH$_3$ desorption step is the rate-determining step during NRR process due to the highest energy barrier demand of 2.15 eV; While the transformation of HNNH$_2$* → H$_2$NNH$_2$* becomes the rate-determining step for the reaction pathway on Fe-ReS$_2$ with a relatively lower energy barrier demand of 0.68 eV. The results indicate that the Fe-doped surface of Fe-ReS$_2$ is beneficial to providing more active sites for highly kinetic NRR process.

Conclusions

In summary, we demonstrate that modulating the energy level of electrocatalysts by low-valent transition-metal doping engineering is an effective strategy to improve the NRR and HER activity of ReS$_2$ based catalysts. By means of electrochemical analysis, in situ FTIR, and DFT studies, we show the introduction of low-valent Fe motifs into ReS$_2$ structures results in the formation of abundant anchor sites for direct adsorption and subsequent activation of N$_2$ molecules, which are responsible for the significantly improved NRR and HER intrinsic activities. Our work unravels the important role of low-valent transition-metal on energy level refining for electrocatalysis optimization, which may also be used in many other catalytic systems.

Supporting Information
Supporting Information is available from the Wiley Online Library or from the author.

Received: ((will be filled in by the editorial staff))
Revised: ((will be filled in by the editorial staff))
Published online: ((will be filled in by the editorial staff))

References

[1] R. Raja, G. Sankar, J. M. Thomas, *J. Am. Chem. Soc.* **2001**, *123*, 8153.

[2] J. W. Erisman, M. A. Sutton, J. Galloway, Z. Klimont, W. Winiwarter, *Nat. Geosci.* **2008**, *1*, 636.

[3] M. A. Legare, G. Belanger-Chabot, R. D. Dewhurst, E. Welz, I. Krummenacher, B. Engels, H. Braunschweig, *Science* **2018**, *359*, 896.

[4] R. Lan, J. Irvine, S. W. Tao, *Int. J. Hydrogen Energy* **2012**, *37*, 1482.

[5] A. Klerke, C. H. Christensen, J. K. Norskov, T. Vegge, *J. Mater. Chem.* **2008**, *18*, 2304.

[6] D. Bao, Q. Zhang, F. L. Meng, H. X. Zhong, M. M. Shi, Y. Zhang, J. M. Yan, Q. Jiang, X. B. Zhang, *Adv. Mater.* **2017**, *29*, 16047993.

[7] N. Zhang, A. Jalil, D. X. Wu, S. M. Chen, Y. F. Liu, C. Gao, W. Ye, Z. M. Qi, H. X. Ju, C. M. Wang, X. J. Wu, L. Song, J. F. Zhu, Y. J. Xiong, *J. Am. Chem. Soc.* **2018**, *140*, 9434.

[8] A. Banerjee, B. D. Yuhas, E. A. Margulies, Y. B. Zhang, Y. Shim, M. R. Wasielewski, M. G. Kanatzidis, *J. Am. Chem. Soc.* **2015**, *137*, 2030.

[9] S. Licht, B. C. Cui, B. H. Wang, F. F. Li, J. Lau, S. Z. Liu, *Science* **2014**, *345*, 637.

[10] C. van der Ham, M. Koper, D. Hetterscheid, *Chem. Soc. Rev.* **2014**, *43*, 5183.

[11] C. X. Guo, J. R. Ran, A. Vasileff, S. Z. Qiao, *Energy Environ. Sci.* **2018**, *11*, 45.

[12] V. Kyriakou, I. Garagounis, E. Vasileiou, A. Vourros, M. Stoukides, *Catal. Today* **2017**, *286*, 2.

[13] Y. Yao, S. Q. Zhu, H. J. Wang, H. Li, M. H. Shao, *J. Am. Chem. Soc.* **2018**, *140*, 1496.

[14] C. Lv, Y. M. Qian, C. S. Yan, Y. Ding, Y. Y. Liu, G. Chen, G. H. Yu, *Angew. Chem. Int. Ed.* **2018**, *57*, 10246; *Angew. Chem.* **2018**, *130*, 10403.

[15] H. K. Lee, C. Koh, Y. H. Lee, C. Liu, I. Y. Phang, X. M. Han, C. K. Tsung, X. Y. Ling, *Sci. Adv.* **2018**, *4*, eaar3208.

[16] Y. C. Hao, Y. Guo, L. W. Chen, M. Shu, X. Y. Wang, T. A. Bu, W. Y. Gao, N. Zhang, X. Su, X. Feng, J. W. Zhou, C. W. Hu, A. X. Yin, R. Si, Y. W. Zhang, C. H. Yan, *Nat. Catal.* **2019**, *2*, 448.

[17] M. F. Wang, S. S. Liu, T. Qian, J. Liu, J. Q. Zhou, H. Q. Ji, J. Xiong, J. Zhong, C. L. Yan, *Nat. Commun.* **2019**, *10*, 341.

[18] F. Qi, X. Q. Wang, B. J. Zheng, Y. F. Chen, B. Yu, J. H. Zhou, J. R. He, P. J. Li, W. L. Zhang, Y. R. Li, *Electrochim. Acta* **2017**, *224*, 593.

[19] J. Gao, L. Li, J. W. Tan, H. Sun, B. C. Li, J. C. Idrobo, C. V. Singh, T. M. Lu, N. Koratkar, *Nano Lett.* **2016**, *16*, 3780.

[20] X. Huang, Z. Zeng, H. Zhang, *Chem. Soc. Rev.* **2013**, *42*, 1934.

[21] J. F. Xie, J. J. Zhang, S. Li, F. Grote, X. D. Zhang, H. Zhang, R. X. Wang, Y. Lei, B. C. Pan, Y. Xie, *J. Am. Chem. Soc.* **2013**, *135*, 17881.

[22] X. D. Zhang, Y. Xie, *Chem. Soc. Rev.* **2013**, *42*, 8187.

[23] L. Zhang, X. Q. Ji, X. Ren, Y. J. Ma, X. F. Shi, Z. Q. Tian, A. M. Asiri, L. Chen, B. Tang, X. P. Sun, *Adv. Mater.* **2018**, *30*, 1800191.

[24] X. D. Li, T. S. Li, Y. J. Ma, Q. Wei, W. B. Qiu, H. R. Guo, X. F. Shi, P. Zhang, A. M. Asiri, L. Chen, B. Tang, X. P. Sun, *Adv. Energy Mater.* **2018**, *8*, 1801357.

[25] Q. Zhang, S. J. Tan, R. G. Mendes, Z. T. Sun, Y. T. Chen, X. Kong, Y. H. Xue, M. H. Rummeli, X. J. Wu, S. L. Chen, L. Fu, *Adv. Mater.* **2016**, *28*, 2616.

[26] S. Tongay, H. Sahin, C. Ko, A. Luce, W. Fan, K. Liu, J. Zhou, Y. S. Huang, C. H. Ho, J. Y. Yan, D. F. Ogletree, S. Aloni, J. Ji, S. S. Li, J. B. Li, F. M. Peeters, J. Q. Wu, *Nat. Commun.* **2014**, *5*, 3252.

[27] S. Horzum, D. Cakir, J. Suh, S. Tongay, Y. S. Huang, C. H. Ho, J. Wu, H. Sahin, F. M. Peeters, *Phys. Rev. B* **2014**, *89*, 15543315.

[28] Z. Cai, D. J. Zhou, M. Y. Wang, S. M. Bak, Y. S. Wu, Z. S. Wu, Y. Tian, X. Y. Xiong, Y. P. Li, W. Liu, S. Siahrostami, Y. Kuang, X. Q. Yang, H. H. Duan, Z. X. Feng, H. L. Wang, X. M. Sun, *Angew. Chem. Int. Ed.* **2018**, *57*, 9392; *Angew. Chem.* **2018**, *130*, 9536.

[29] S. H. Ye, Z. X. Shi, J. X. Feng, Y. X. Tong, G. R. Li, *Angew. Chem. Int. Ed.* **2018**, *57*, 2672; *Angew. Chem.* **2018**, *130*, 2702.

[30] Y. Shi, Y. Zhou, D. R. Yang, W. X. Xu, C. Wang, F. B. Wang, J. J. Xu, X. H. Xia, H. Y. Chen, *J. Am. Chem. Soc.* **2017**, *139*, 15479.

[31] F. L. Lai, J. R. Feng, X. B. Ye, W. Zong, G. J. He, Y. E. Miao, X. M. Han, X. Y. Ling, I. P. Parkin, B. C. Pan, Y. F. Sun, T. X. Liu, *J. Mater. Chem. A* **2019**, *7*, 827.

[32] F. L. Lai, D. Y. Yong, X. L. Ning, B. C. Pan, Y. E. Miao, T. X. Liu, *Small* **2017**, *13*, 1602866.

[33] C. M. Corbett, C. Mcclellan, A. Rai, S. S. Sonde, E. Tutuc, S. K. Banerjee, *ACS Nano* **2015**, *9*, 363.

[34] J. Gao, L. Li, J. W. Tan, H. Sun, B. C. Li, J. C. Idrobo, C. V. Singh, T. M. Lu, N. Koratkar, *Nano Lett*. **2016**, *16*, 3780.

[35] Y. Liu, Y. Su, X. Quan, X. F. Fan, S. Chen, H. T. Yu, H. M. Zhao, Y. B. Zhang, J. J. Zhao, *ACS Catal.* **2018**, *8*, 1186.

[36] A. P. Grosvenor, B. A. Kobe, M. C. Biesinger, N. S. McIntyre, *Surf. Interface Anal.* **2004**, *36*, 1564.

[37] K. Ataka, T. Yotsuyanagi, M. Osawa, *J. Phys. Chem.* **1996**, *100*, 10664.

[38] S. D. Lin, A. C. Gluhoi, B. E. Nieuwenhuys, *Catal. Today* **2004**, *90*, 3.

[39] L. K. Xu, Y. L. Xin, J. T. Wang, *Electrochim. Acta* **2009**, *54*, 1820.

[40] G. Ramis, L. Yi, G. Busca, M. Turco, E. Kotur, R. J. Willey, *J. Catal.* **1995**, *157*, 523.

[41] Y. Ikezawa, T. Sawatari, T. Kitazume, H. Goto, K. Toriba, *Electrochim. Acta* **1998**, *43*, 3297.

[42] W. Gulaczyk, M. Kreglewski, A. Valentin, *J. Mol. Spectrosc.* **2003**, *220*, 132.

[43] J. H. Montoya, C. Tsai, A. Vojvodic, J. K. Norskov, *ChemSusChem* **2015**, *8*, 2180.

[44] X. Ma, J. Liu, H. Xiao, H. Li, M. H. Shao, *J. Am. Chem. Soc*. **2018**, *140*, 46.

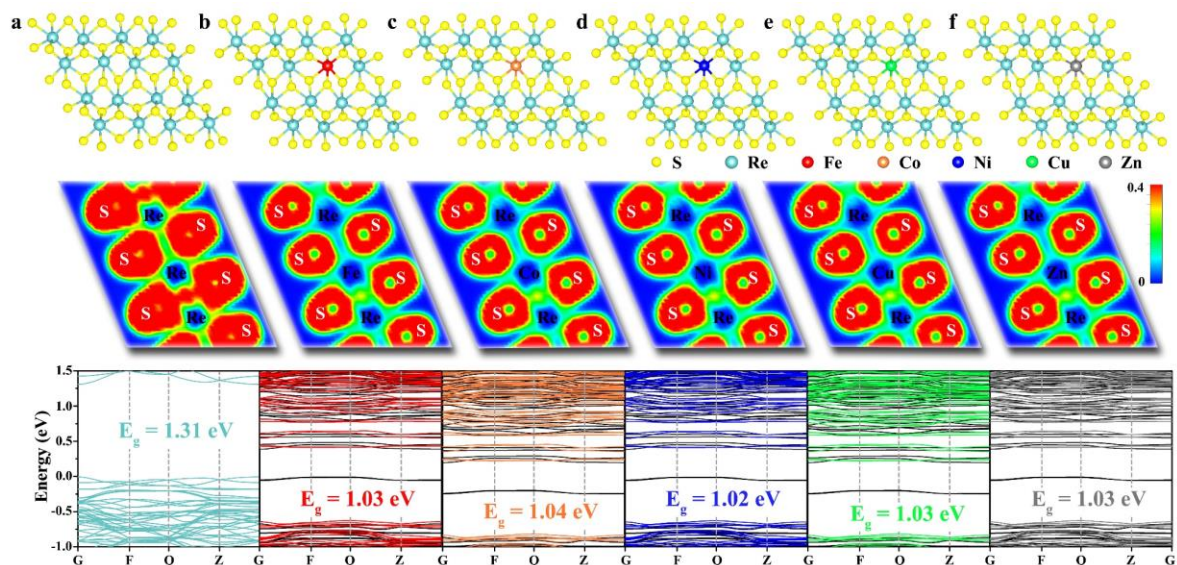[45] J. X. Zhao, Z. F. Chen, *J. Am. Chem. Soc*. **2017**, *139*, 12480.

Figure 1. Atomistic models of crystal structure, two dimensional electron localization function (ELF) mappings, and calculated band structures for (a) ReS_2, (b) $Fe-ReS_2$, (c) $Co-ReS_2$, (d) $Ni-ReS_2$, (e) $Cu-ReS_2$, and (f) $Zn-ReS_2$, respectively.
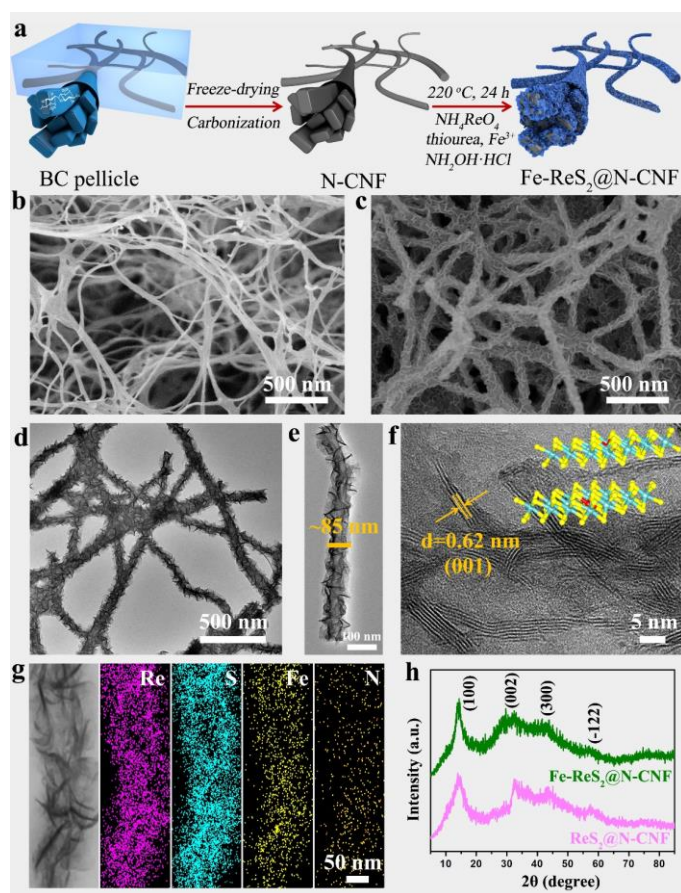
Figure 2. (a) Schematic illustration of preparation process of Fe-ReS$_2$@N-CNF. SEM images of (b) N-CNF and (c) 5 mol % Fe-doped ReS$_2$@N-CNF (Fe-ReS$_2$@N-CNF-5). (d-e) TEM images, (f) HRTEM image, and (g) corresponding element mapping of Fe-ReS$_2$@N-CNF-5. (h) XRD patterns of Fe-ReS$_2$@N-CNF-5 and ReS$_2$@N-CNF.
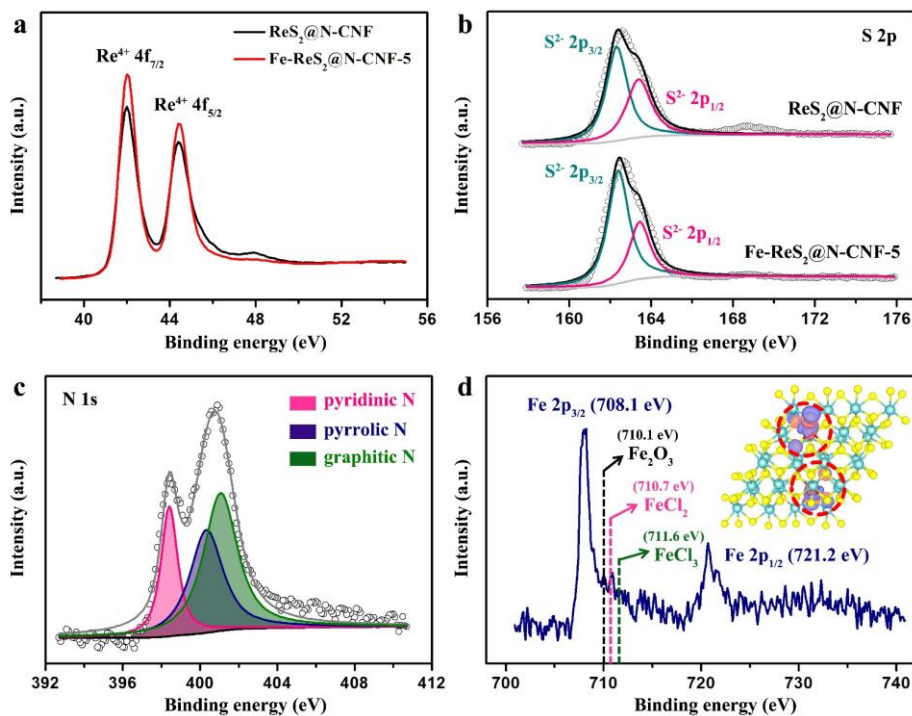
Figure 3. High-resolution XPS spectra of (a) Re 4f and (b) S 2p peaks for Fe-ReS$_2$@N-CNF-5 and ReS$_2$@N-CNF, respectively. High-resolution XPS spectra of (c) N 1s and (d) Fe 2p for Fe-ReS$_2$@N-CNF-5.
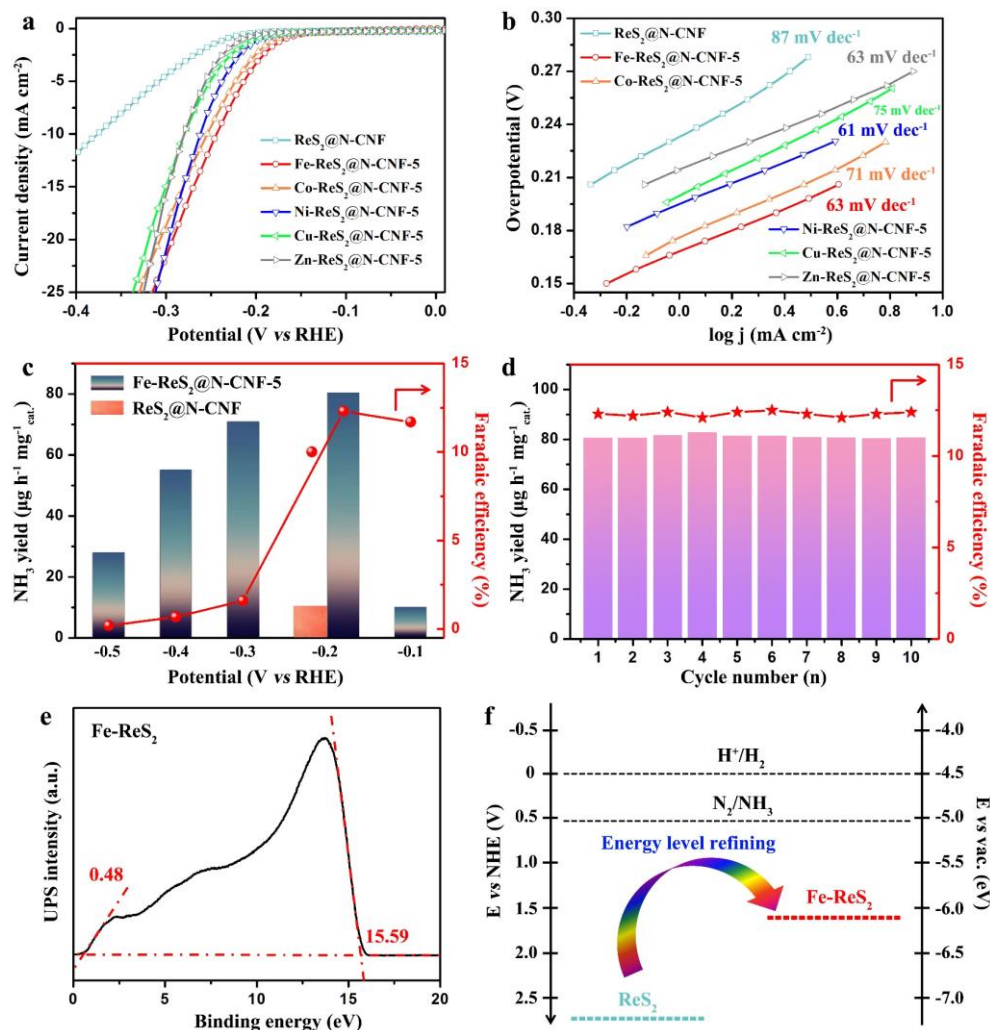
Figure 4. Electrocatalytic HER/NRR of 5 mol % transition-metal doped ReS_2 nanosheets wrapped nitrogen-doped carbon nanofiber (Fe/Co/Ni/Cu/Zn-ReS_2@N-CNF-5) and non-doped ReS_2@N-CNF catalysts in aqueous solution of 0.1 M Na_2SO_4 under ambient conditions. (a) Polarization curves. (b) Tafel curves. (c) The NH_3 production rates (bar graph) and FE_{NH3} (red line) of Fe-ReS_2@N-CNF-5 and ReS_2@N-CNF at different potentials. (d) NRR stability test of Fe-ReS_2@N-CNF-5 at -0.2 V versus. RHE. (e) Ultraviolet photoelectron spectroscopy (UPS) spectra of Fe-ReS_2 nanosheets. (f) Band structure diagram for Fe-ReS_2 and pure ReS_2.
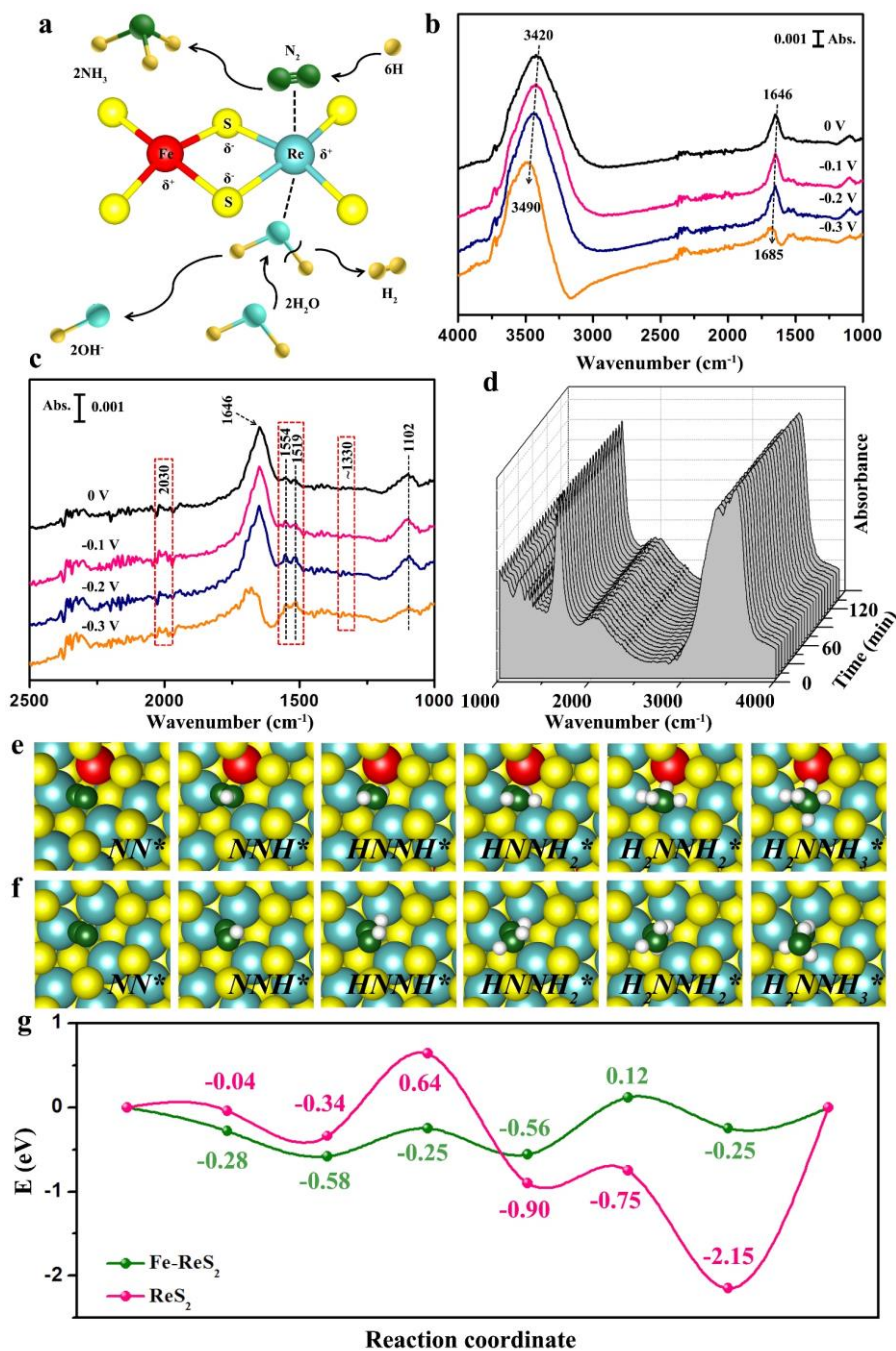
Figure 5. (a) The proposed mechanism on uncoordinated Fe (δ^+) and Re (δ^+) centers during NRR and HER processes. (b) In-situ SEIRAS spectra from 0 to -0.3 V on the Fe-ReS$_2$@N-CNF-5 catalyst in a N$_2$-saturaed 0.1 M Na$_2$SO$_4$ solution. (c) Amplification of the selected area in (b). (d) Time-dependent SEIRAS spectra of Fe-ReS$_2$@N-CNF-5 catalyst at a voltage of -0.2 V. Optimized structures of NH*, NNH*, HNNH*, HNNH$_2$*, H$_2$NNH$_2$*, and H$_2$NNH$_3$ intermediates on: (e) Fe-ReS$_2$ and (f) ReS$_2$. (g) Free energy diagram of NRR to NH$_3$ on Fe-ReS$_2$ and ReS$_2$.

Feili Lai, Nan Chen, Xiaobin Ye, Guanjie He, Wei Zong, Katherine B. Holt, Bicai Pan, Ivan P. Parkin, Tianxi Liu,* Renjie Chen*

Refining Energy Levels in ReS$_2$ Nanosheets by Low-Valent Transition-Metal Doping for Dual-Boosted Electrochemical Ammonia/Hydrogen Production

ToC figure